Geotechnical Testing Journal

Erick Baziw[1] and Gerald Verbeek[1]

Signal Processing Challenges When Processing DST and CST Seismic Data Containing TIRs

Erick Baziw[1] and Gerald Verbeek[1]

Signal Processing Challenges When Processing DST and CST Seismic Data Containing TIRs

ABSTRACT

Downhole Seismic Testing (DST) and Crosshole Seismic Testing (CST) are important geotechnical testing techniques which provide for low strain ($<10^{-5}$) in situ compression (Vp) and shear (Vs) wave velocity estimates. The Vs and Vp interval velocities are determined by obtaining relative arrival times of source waves as they travel through the stratigraphy and are recorded by one or more vertically (DST) and/or horizontally (CST) offset seismic sensors. The relative arrival times are typically obtained by cross-correlating the recorded source waves or identifying reference features within the seismic trace such as a peak, trough, crossover point, or first break. A very common and yet poorly understood problem encountered in DST and CST is the analysis of seismograms that contain Total Internal Reflections (TIRs). TIRs arise when the incident angle exceeds the critical angle; as a result of which reflection coefficients become complex, which in turn leads to distortions in the reflected source wave. This paper addresses the issue of TIRs and the signal processing challenges when processing seismic data containing TIRs.

Introduction

A fundamental goal of geotechnical in situ testing is the accurate estimation of the shear and compression wave velocities (V_S and V_P, respectively) in the ground. These parameters form the core of mathematical theorems to describe the elasticity/plasticity of soils and they are used to predict the soil response (settlement, liquefaction or failure) to imposed loads (whether from foundations,

FIG. 1   Schematic of the typical DST configuration.

FIG. 2   Schematic of the typical CST configuration.
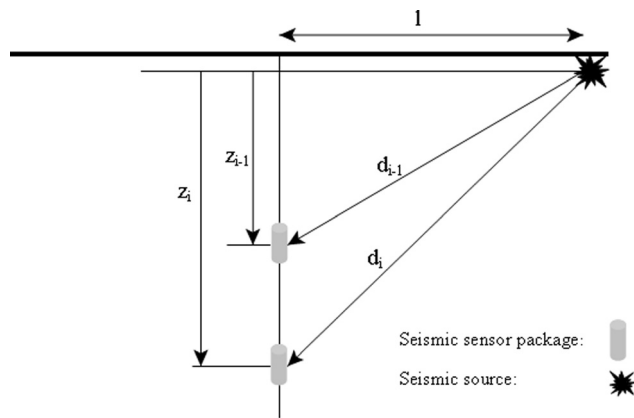
heavy equipment, earthquakes or explosions) (Finn 1984; Andrus et al. 1999, 2000; Ishihara 1982). Accuracy in the estimation of shear and compression wave velocities is of paramount importance because these values are squared during the calculation of various geotechnical parameters such as the Shear Modulus (G), Poisson's Ratio (μ), and Young's modulus (E). For example, from elasticity theory we know that the formula for the maximum shear modulus is $G_0 = \rho V_S^2$, where ρ is the soil density and V_S is the shear wave velocity.

The two dominant geotechnical techniques for measuring in-situ V_S and V_P velocities are the Downhole Seismic Test (DST) such as the Seismic Cone Penetration Test (SCPT) (Campanella et al. 1986; Baziw 1993), and the Crosshole Seismic Test (CST) (Ballard 1976))[2]. In both cases, the main goal is to obtain relative arrival times as the source wave travels through the soil profile of interest, and from these relative arrival times the V_S and V_P velocities are then calculated.

Figure 1 shows a schematic of the typical DST configuration: a seismic source is used to generate a seismic wave train at the ground surface. One or more downhole seismic receivers are used to record the seismic wave train at predefined depth increments. The downhole receiver(s) may be positioned at selected test depths in a borehole or advanced as part of an instrumentation package as in the case of SCPT. When triggered by the seismic source a data recording system records the response of the downhole receiver(s). DST is predominantly utilized for determining interval velocity profiles (for both V_S and V_P) by measuring the relative travel times between the source waves recorded at subsequently greater depths. For example, in **Fig. 1**, the interval velocity, V_i, between depth increments z_i and z_{i-1} is given as[3]

$$(1) \qquad V_i = (d_i - d_{i-1})/(t_i - t_{i-1})$$

[2]ASTM Standards D7400-08 and D4428/D4428M-07 provide thorough outlines of the DST and CST equipment and methodologies, respectively.
[3]Assuming straight ray propagation between source and receiver.
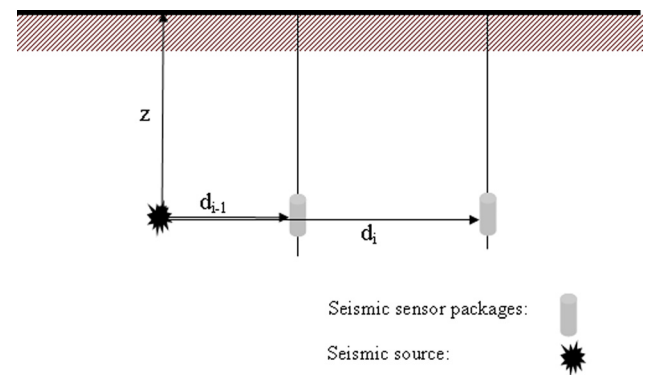
where t_i and t_{i-1} are the arrival times of the source wave at depths z_i and z_{i-1}, respectively. For more sophisticated (and likely more accurate) solutions, ray path refraction can be taken into account by implementing iterative forward modeling or data inversion techniques (Baziw 2002; Baziw and Verbeek 2012).

CST is very similar to DST, but in this case the seismic sensors are offset laterally as opposed to vertically. **Figure 2** shows a schematic of the typical CST configuration: a seismic source is used to generate a seismic wave train downhole within a borehole. One or more crosshole seismic receivers are used to record the seismic wave train at predefined lateral offsets at a constant depth. In **Fig. 2**, the interval velocity, V_i, between lateral increments d_i and d_{i-1} and depth z_i is similarly given as Eq 1, where t_i and t_{i-1} denote the arrival times of the source wave at lateral offsets d_i and $d_{i-1,}$ respectively.

In both DST and CST investigations, there are site conditions that result in source high energy wave multiples referred to as Total Internal Reflections (TIRs). These multiples complicate the recorded time series making the estimation of interval relative arrival times a very difficult task. TIRs are typical in CST investigations (since horizontally travelling source waves have high angles of incidence on bounding stratigraphic layers), while in DST investigations TIRs are encountered whenever there are significant man-made structures nearby the test location (e.g., foundation piles, stone columns, or deep underground structures such as deep basements, parking garages, and dam structures).

When dealing with TIRs, it is of paramount importance to first understand the structure and form of the recorded seismograms prior to blindly applying signal processing algorithms on acquired data. Once there is a clear understanding of the recorded seismograms, it will become obvious that the standard analysis methods will not generate reliable results, which will be illustrated not only by a review of the theoretical background, but also by examples using both simulated and actual field data.

Standard Techniques for Obtaining Relative Arrival from DST and CST

The techniques typically employed in obtaining the relative arrival times outlined in Eq 1 are either.

1. Techniques that rely upon identifying reference points or markers within the seismograms.
2. Techniques that implement the cross correlation function or cross-power spectrum.

Figure 3 outlines (Amini 2006) typical time markers utilized for a SH-wave reverse polarity investigation in SCPT, which are identified as the first peak (2), first crossover (C), second peak (3), and second crossover (D). The preferred techniques in obtaining the relative arrival times are the implementation of the cross correlation function or cross-power spectrum.

The cross correlation between two time or distance offset seismograms is given as
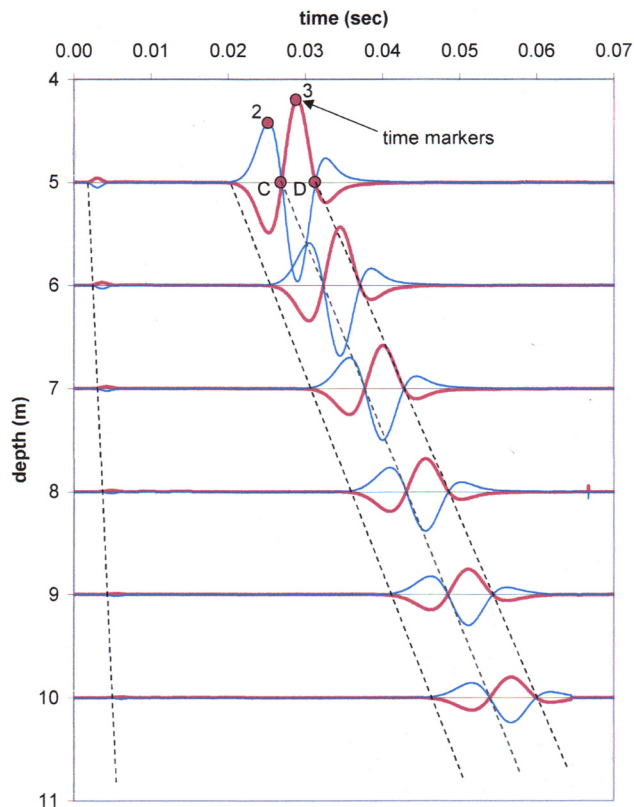
(2)
$$\varphi_{xy}(\tau) = \sum_k X_k Y_{k+\tau}$$

where:

$\varphi_{xy}(\tau) =$ the cross correlation function,
$Y_k =$ the sampled data at distance 1 and at sample time k,

FIG. 3 Typical reversely polarized DST data with time markers (Amini 2006)).

$X_k =$ the sampled data at distance 2 at sample time k, and
$\tau =$ the time shift between the two sets of recorded waves (note: distance 2 > distance 1).

The value of the time shift at the maximum cross correlation value is assumed to be the relative travel time difference, Δt, for the source wave to travel the distance increment.

This technique has the following advantages (Baziw 1993, 2002) over selecting time markers within the seismogram:

- The human bias associated with visually selecting a reference point or time marker is minimized.
- The full waveform is utilized in deriving interval travel times as opposed to a single point.
- The correlation coefficient between the two waves can be used as a velocity accuracy estimate. This parameter gives the investigator an indication of the similarity between the two waves being correlated and the subsequent accuracy of the velocity estimate.

The Fourier transform of the cross correlation gives the cross-power spectrum ($\emptyset_{xy}(f)$, where f denotes frequency in Hz). This can also be derived from the Fourier transforms of the two traces under analysis as follows:

(3)
$$\emptyset_{xy}(f) = S_x(f)S_y^*(f)$$

where:

$S_x(f)$ and $S_y(f) =$ the Fourier transform of traces X and Y, respectively, and
$* =$ the complex conjugate of the Fourier transform.

The cross-power spectrum allows for the determination of the coherence, $C(f)$, a real function with a value between zero and one, which shows the correlation between seismic traces X and Y at each frequency. The real part of cross-power spectrum, $\emptyset_{xy}^R(f)$, is termed the cospectrum, while the imaginary part, $\emptyset_{xy}^I(f)$, is termed the quadrature spectrum (Kanasewich 1981). The coherence is given as

(4)
$$C_{xy}(f) = \frac{\left(\emptyset_{xy}^R(f)\right)^2 + \left(\emptyset_{xy}^I(f)\right)^2}{\emptyset_{xx}(f)\emptyset_{yy}(f)}$$

where $\emptyset_{xx}(f)$ and $\emptyset_{yy}(f)$ denote the auto-power spectra of seismic traces X and Y, respectively. The autocorrelation function is obtained with Eq 2 with $X_k \equiv Y_k$. The Fourier transform of the autocorrelation provides the auto-power spectra, which are real functions due to the fact that the autocorrelation is zero phase.
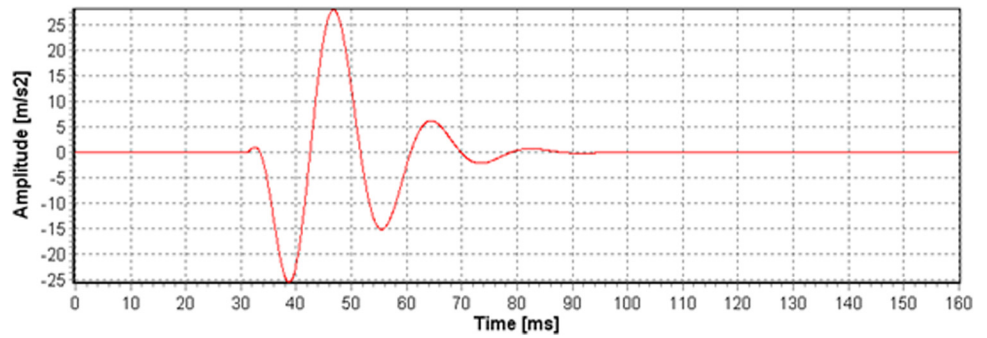
The phase spectrum is given by

(5)
$$\theta_{xy}(f) = \tan^{-1}\left(\frac{\emptyset_{xy}^I(f)}{\emptyset_{xy}^R(f)}\right)$$

Robinson and Treitel (1980) outline that the absolute value of the cross-power spectrum is less than or equal to the geometric mean of the individual auto-power spectra. This property is mathematically represented as

FIG. 4

Berlage source wave with dominant frequency of 55 Hz and recorded at depth 5 m.

(6)
$$|\emptyset_{xy}(f)| \leq \sqrt{|\emptyset_{xx}(f)||\emptyset_{yy}(f)|}$$

From Eq 6, it is evident that the cross-power spectrum only retains the common frequencies of traces X and Y.

If the time offset set is less than one full waveform period (i.e., $\theta_{xy}(f) < 360°$) then the relative arrival time derived from the cross-spectrum is given as

(7)
$$\Delta t = \theta_{xy}(f)/2\pi f$$

For example, if the dominant frequency of a seismic signal is 80 Hz then the period, T, is 1/80 s or 12.5 ms. If a phase at this frequency is calculated to be 110° (1.92 rads) then the relative arrival time between the two source waves recorded away from the seismic source is calculated with Eq 7 as

(8)
$$\Delta t = 1.92/2\pi(80) = 0.00382 \text{ s} = 3.82 \text{ ms}$$

This makes intuitive sense due to the fact that a phase of 110° is equivalent to $(110°/360°)T = 0.306\,T = 3.82$ ms.

The ability to estimate relative arrival times for phases that exceed 360° is more challenging. In this case, the investigator will have to apply a correction based upon the estimated dominant frequency. For example, if two signals with a dominant frequency of 80 Hz are offset by 40 ms then the phase can be calculated with Eq 7 as

(9)
$$\theta_{xy}(80) = \Delta t \times 2\pi f = 0.040 \times 160\pi = 20.106 \text{ radians or } 1152°$$

However, instead of 1152° or 3.2 T, the Fourier transform would generate a value less than 360°, or in this particular case a phase equal to $0.2 \times 360° = 72°$ or 1.257 radians. The investigator has to apply a correction by specifying that an additional $3T$ or $3 \times 360° = 1080°$ or 18.850 rads of phase has occurred, which then allows the total relative travel time to be calculated as follows:

(10)
$$\Delta t = ((1.257 + 18.850)/2\pi(80)) = 0.04 \text{ s or } 40 \text{ ms}$$

In a typical analysis, the cross-power spectrum is determined via the Fast Fourier Transform (FFT) (Williams et al. 2007). The phase is then calculated at one or more specific frequencies when the corresponding coherency at that frequency exceeds a user specified amount (typically 0.7 or 0.8). It should be noted that, as pointed out above, the phase estimate provided by the FFT is the phase relative to the start of the time-domain signal (and therefore should be adjusted to get the actual phase, as shown above) and that the FFT returns the negative counterpart (the so-called "phase lag") of the phase (e.g. $-288°$ instead of 72°).

The cross-power spectrum is susceptible to frequency domain estimation concerns of "leakage" due to inadequate frequency resolutions (directly related to the number of samples
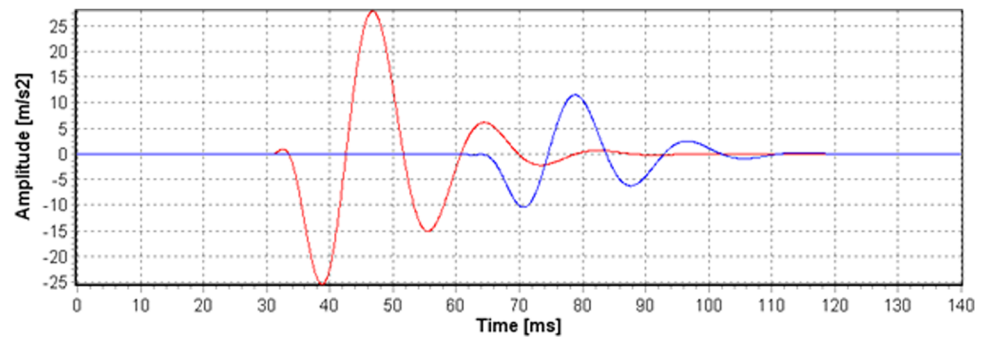
FIG. 5

Source Wave 2 (lower amplitude trace) superimposed on Source Wave 1 without time offset.
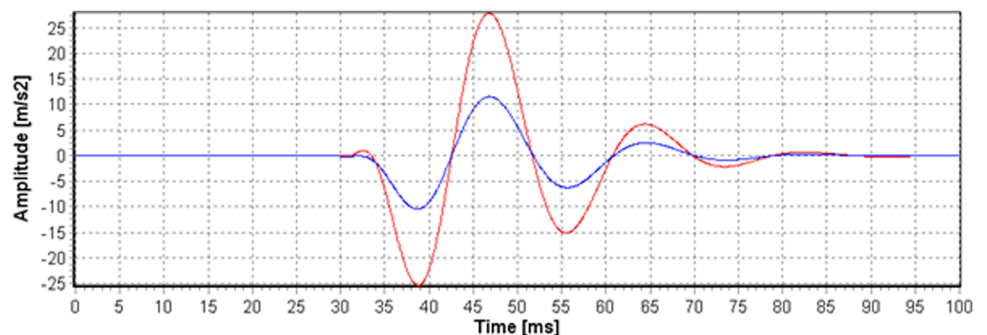
FIG. 6

Source Wave 2 (lower amplitude trace) superimposed on Source Wave 1 with 32 ms time offset.

within the seismic time series), data truncation and edge effects (Kanasewich 1981). The recorded seismic source wave can be considered as a finite length of data within the recorded seismogram. With respect to the FFT, a finite duration source is analogous to multiplying the source with a box car function, which results in distortions (so-called "ringing") in the frequency domain. Source waves with lengths that are not multiples of the dominant source wave frequency will also experience "edge effects," which also result in frequency distortions. These distortions are typically minimized by tapering the source wave by applying cosine bells (Kanasewich 1981) in the time domain.

Finally, as pointed out by Amini (2006), relative arrival time estimates derived from the cross-power spectrum phase are advantageous for cases where the damping ratio of the soil is relatively large (>5 %). And even for a damping ratio of 5 %, Amini (2006) has shown that interval velocities estimates from the cross correlation function are within 1 % of the true value.

NUMERICAL EXAMPLE

To illustrate the above the Berlage source wave (Baziw 2006, 2007, 2011) illustrated in **Fig. 4** is processed. This source wave has a dominant frequency of 55 Hz, a sampling rate of $\Delta = 0.05$ ms, and is assumed to be recorded during a DST at a vertical depth of 5 m where the source is assumed to have a radial offset from the vertical of 1.5 m.

Another Berlage source wave is simulated and is assumed to be recorded at a depth of 10 m. This wave was generated by assuming a soil layer with an absorption Q value of 30 1/Np[4] (Sheriff and Geldart 1982), a relative geometric spreading value of 0.5 and a relative arrival time of 32 ms. **Figure 5** shows these two waves superimposed without a time offset, while in **Fig. 6** a time offset of 32 ms has been applied. **Figure 7** then illustrates the normalized output after applying Eq 2 on the traces illustrated in **Fig. 6**. As is shown in **Fig. 7**, the peak of the cross correlation function occurs at 32 ms, which matches the applied time offset.

[4] 1 Np (nepers) = 8.69 dB or 1 dB = 0.115 Np.

In **Fig. 8**, the Fourier transform (cross-power spectrum) is given of the cross correlation function shown in **Fig. 7**. From **Fig. 8**, it appears that the dominant frequency is 53.8 Hz, while in reality it is 55 Hz as mentioned before. This deviation or "leakage" is to be expected in this case given the low Frequency Resolution (FR) of the cross correlation, which is given as

$$FR = 1/(N \times \Delta)$$

where:

N = the length of the cross correlation function, and

Δ = the sampling interval.

In this case $N = 4096$ and $\Delta = 0.05$ ms, which means that FR is 4.88 Hz.

By applying Eq 4 on the cross power spectrum shown in **Fig. 8**, the coherency is calculated and the results are shown in **Fig. 9**. For the data points where the coherency exceeds 0.7, the cross-power phase estimates are calculated by applying Eq 5 and the results are shown in **Fig. 10**.

Applying Eq 7 to this test case results in a phase of $\theta_{xy}(55) = \Delta t 2\pi f = 11.06$ radians or 633.7° (since $\Delta t = 32$ ms and $f = 55$ Hz); therefore, we would expect an estimated phase value from the cross-power spectrum at 55 Hz of 633.7° − 360° = 273.7° (or − 84.3°). **Table 1** outlines the cross-power phase estimation results illustrated in **Fig. 10** with the associated relative arrival time estimates (Δt^1) obtained by implementing Eq 7 on the raw value for the phase estimate (i.e., $\theta_{xy}(f) < 360°$), the arrival time estimate (Δt^2) for the one period correction ($T = 1/f$), and the overall relative arrival time estimate ($\Delta t = \Delta t^1 + \Delta t^2$). As is evident from **Table 1**, the interval velocities obtained from the cross-power phase are nearly identical to the true value of 32 ms.
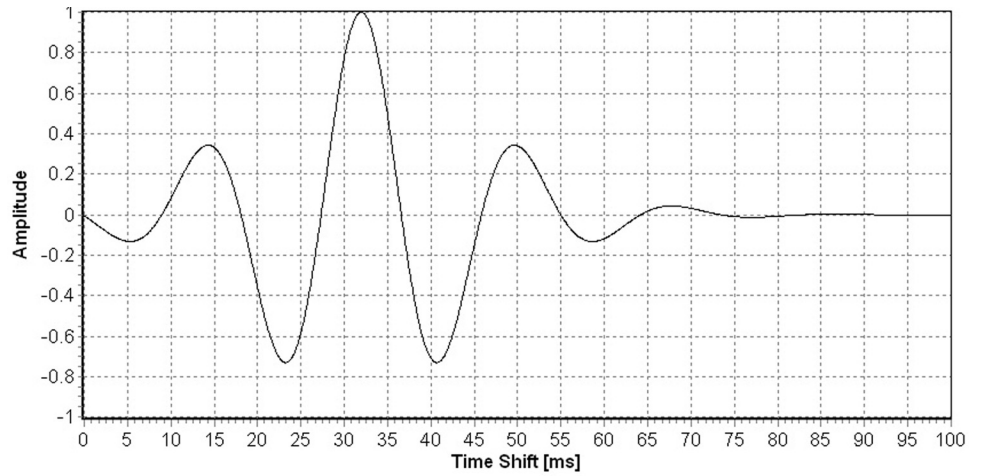
Physics and Governing Mathematical Equations of TIRs

The physics and governing mathematical equations of TIRs (Shearer 1999; Sheriff and Geldart 1982; Aki and Richards 2002; Fokkema and Ziolkowski 1987) are illustrated by considering a
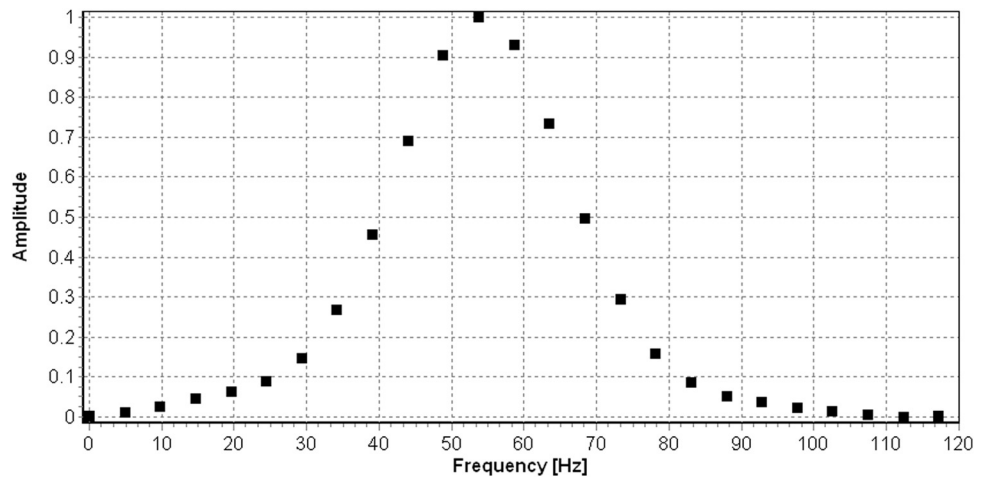
FIG. 7

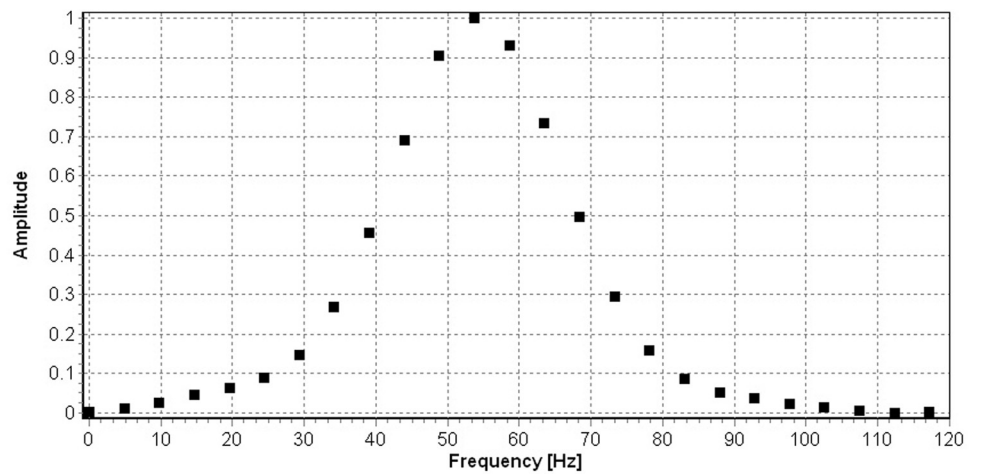Normalized auto-correlation of the Source Wave 2 superimposed on Source Wave 1.

FIG. 8

FFT normalized amplitude spectrum (cross-power spectrum) of cross correlation function illustrated in **Fig. 7**.
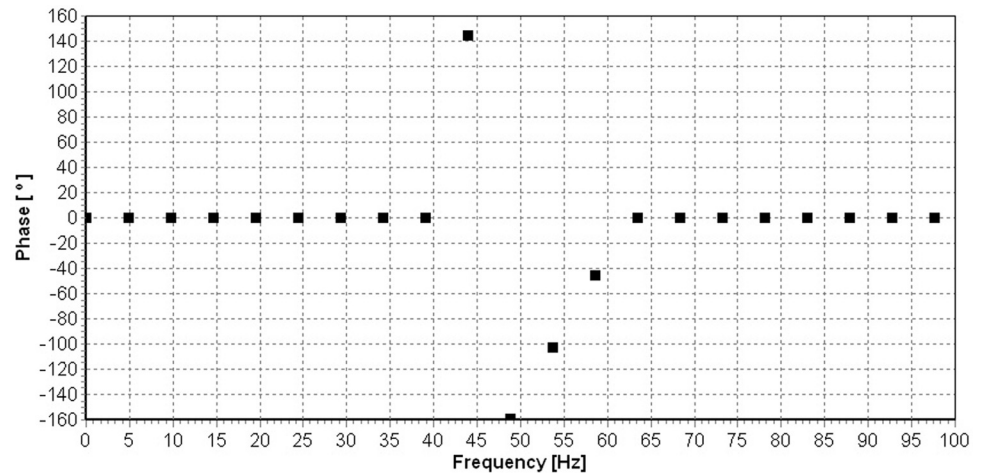

FIG. 9

Coherency of cross-power spectrum illustrated in **Fig. 8**.

FIG. 10

Phase estimates for cross-power spectrum illustrated in **Fig. 8**. Phase values are calculated when the coherency shown in **Fig. 9** exceeds 0.7 at a specific frequency.

horizontally polarized (SH-wave) DST investigation within concrete piles or stone columns, but the concepts outlined are directly applicable to a CST being carried out in strata with significant impedance mismatches as illustrated in **Fig. 11**. **Figure 12** outlines a schematic of the SH-wave SCPT investigation that is being carried out, whereby the SH-wave velocity of the piles/stone columns (V_2) is much greater than that of the surrounding soil (V_1). In **Fig. 12**, ρ is the medium density, **3** denotes the first arriving direct SH source wave, while **1** and **2** denote the reflecting waves, θ_1 denotes the incident and reflecting angles, θ_2 is the refraction angle, and $\beta_1 = 90° - \theta_1$.

GOVERNING EQUATIONS

Snell's Law:

(11)
$$\frac{\sin \theta_2}{V_2} = \frac{\sin \theta_1}{V_1} = p$$

- If V_2 is less than V_1, then θ_2 is less than θ_1. As V_2 approaches 0 (air/ground or water/ground interface), then $\theta_2 = 0°$. In Eq 11, p is termed the *ray parameter* and denotes the horizontal slowness of the ray.
- The critical angle, Φ, is defined as the angle where $\theta_2 = 90°$ and the refracted (head / conical) wave is travelling along the interface. For angles of incidence greater

than Φ, it is impossible to satisfy Snell's law (using real angles) since $\sin(\theta_2)$ cannot exceed unity and consequently internal reflections occur. This does not mean, however, that 100 % of the energy is reflected:

1. In case of an incident P-wave, a small portion of the energy is converted into S-waves and evanescent waves.
2. In case of an incident SV-wave, a small portion of the energy is converted into P-waves and evanescent waves.
3. In case of an incident SH-wave, a small portion of the energy is converted into evanescent waves.

- There are high incident angles between the reflecting piles and/or stone columns. Moreover, the velocity contrast is quite large ($V_2 \gg V_1$), and therefore the critical angle will be relatively small as is clear from Eq 11, which defines the critical angle:

(12)
$$\Phi = \sin^{-1}(V_1/V_2)$$

If we assume that $V_2 = 2V_1$, the critical angle is 30°. As V_2 increases even more, the critical angle becomes even smaller, and we can therefore safely assume that the incident angles will exceed the critical angle.

TABLE 1   Interval velocities derived from estimated cross-power phases.

Frequency (Hz)	Phase (°)	Phase (radians)	Δt^1 (Eq 7) (ms)	Δt^2 ($T = 1/f$) (ms)	$\Delta t = \Delta t^1 + \Delta t^2$ (ms)	Error[a] (%)
44	−215.1° or 144.9°	2.53	9.1	22.7	31.8	6
48.8	−160° or 200°	3.49	11.4	20.4	31.8	6
53.9	−100° or 260°	4.54	13.4	18.6	32	0
58.6	−45.2° or 314.8°	5.49	14.9	17.1	32	0

[a]Error = (Estimate—true)x100/true.

FIG. 11   Schematic of CST configuration illustrating source wave reflection.

FIG. 12   Cross-section of SCPT illustrating direct and reflecting source waves.
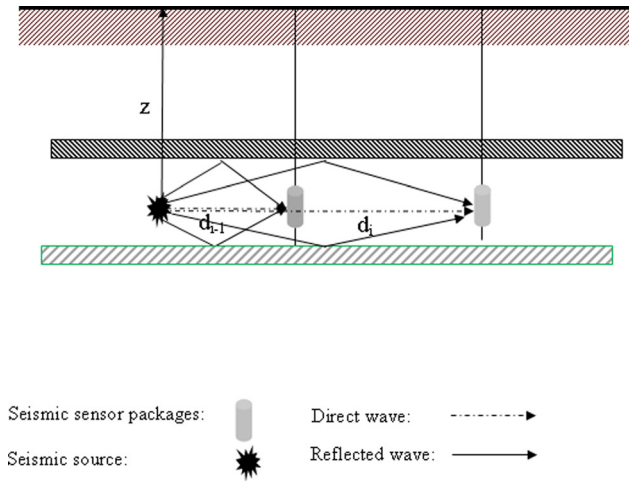
SH-WAVE REFLECTION AND TRANSMISSION COEFFICIENTS

The SH *precritical reflection coefficients* (reflections at angles less than the critical angle) are given as

$$(13) \quad R = \frac{A_1}{A_0} = \frac{G_1\eta_1 - G_2\eta_2}{G_1\eta_1 + G_2\eta_2} = \frac{\rho_1 V_1 \cos\theta_1 - \rho_2 V_2 \cos\theta_2}{\rho_1 V_1 \cos\theta_1 + \rho_2 V_2 \cos\theta_2}$$

$$(14) \quad T = \frac{A_2}{A_0} = \frac{2G_1\eta_1}{G_1\eta_1 + G_2\eta_2} = \frac{2\rho_1 V_1 \cos\theta_1}{\rho_1 V_1 \cos\theta_1 + \rho_2 V_2 \cos\theta_2}$$

where:

R = the reflection coefficient,

T = the transmission coefficient,

A_0 = the amplitude of incident wave,

A_1 = the amplitude of reflected wave,

A_2 = the amplitude of refracted wave (note: $Z_i = \rho_i V_i$ is the *acoustic impedance*),

G_i = the shear modulus of medium i (note $G = \rho V_s^2$), and

η_i = the horizontal slowness within medium i for the example illustrated in **Fig. 12** (note that η_i would be the vertical slowness for a horizontal interface). The latter can be given as:

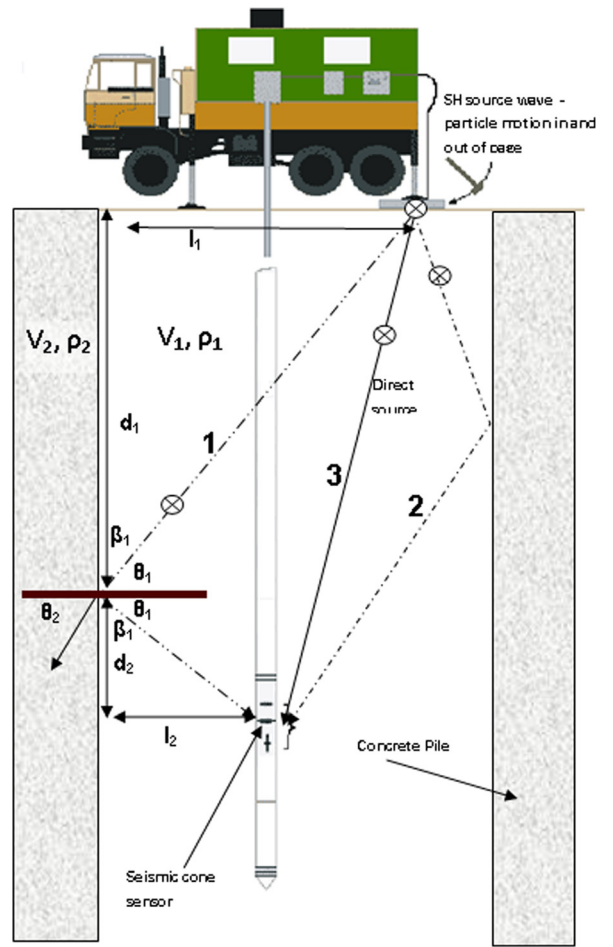$$(15a) \quad \eta_1 = u_1 \cos\theta_1 = \cos\theta_1 / V_1 = \sqrt{u_1^2 - p_1^2}$$

$$(15b) \quad \eta_2 = u_2 \cos\theta_2 = \cos\theta_2 / V_2 = \sqrt{u_2^2 - p_2^2}$$

To meet boundary conditions (i.e., abide by Snell's Law) it is required that $p = p_1 = p_2$ in Eqs 15a and 15b.

At the *critical angle*, which as mentioned earlier is defined as the angle where $\theta_2 = 90°$, $\sin\theta_2 = 1$ and $\cos\theta_2 = 0$; therefore, using Eqs 11, 13, 14, and 15b:

- the ray parameter $p = u_2$
- the reflection coefficient $R = 1$
- the transmission coefficient $T = 2$
- the slowness in medium 2 $\eta_2 = 0$

This means that the transmitted SH wave has an amplitude equal to twice that of the incident wave and travels along the interface (also termed a Head Wave), while the reflected wave has the same amplitude as the incident wave, and there is no vertical transmission[5].

Beyond the *critical angle*, θ_2 becomes complex. This becomes evident when Eq 11 is rewritten as

$$(16) \quad \theta_2 = \sin^{-1}\left(\frac{V_2}{V_1}\sin\theta_1\right)$$

Since $V_1 < V_2$, the arcsin function can become greater than 1, which results in a complex solution for θ_2. Consequently, η_2 is imaginary, and transmitted waves with imaginary slowness are termed *evanescent waves*. Evanescent waves have no vertical energy flux where the energy normalized transmission coefficient is zero and their amplitude decays exponentially with depth.

---

[5]Continuity of displacement requires $A_0 + A_1 = A_2$. The sum of the energy flux density on the interface from all of the scattered waves must equal the energy flux density from the incident waves.

Since any incident angle greater than the critical angle will be largely reflected from the boundary instead of being refracted, *post-critical angle* reflections are referred to as TIRs due to the fact that a negligible amount of energy is transmitted and nearly all of the energy reflected.

The SH *post-critical reflection coefficient* can then be given as

$$(17) \qquad R = \frac{A_1}{A_0} = \frac{G_1\eta_1' - iG_2\eta_2'}{G_1\eta_1' + iG_2\eta_2'} = \frac{e^{-i\alpha}}{e^{+i\alpha}} = e^{-i2\alpha}$$

with

$$(18) \qquad \alpha = \tan^{-1}\left(\frac{G_2\eta_2'}{G_1\eta_1'}\right)$$

where:

$i =$ the imaginary number, and

η_1' and η_2' the *post-critical* vertical slowness within mediums 1 and 2, respectively, which can be given as:

$$(19a) \qquad \eta_1' = \sqrt{u_1^2 - p^2}$$

$$(19b) \qquad \eta_2' = \sqrt{p^2 - u_2^2}$$

The seismogram for TIRs is generated by convolving the source waves by the reflection coefficients given in Eq 17 for various incident angles that exceed the critical angle. In the frequency domain, this is equivalent to multiplying the source wave by the reflection coefficients given by Eq 17, producing a frequency-independent phase shift as shown below:

$$
\begin{aligned}
(20) \qquad U &= RA_0 e^{i(kx-\omega t)} \\
&= A_0 e^{-i2\alpha} e^{i(kx-\omega t)} \\
&= A_0 e^{i(kx-\omega(t+2\alpha/\omega))}
\end{aligned}
$$

where:

$k =$ the wave number,

$x =$ the distance,

$\omega =$ the angular frequency, and

$t =$ the time.

As is evident from Eq 20, the reflected wave has a phase shift of $2\alpha/\omega$ or $2\alpha/2\pi f_d$, where f_d is the dominant frequency of the source wave.

It can be shown (Aki and Richards 2002) that any phase shift of a source wave can be determined from the source wave and its Hilbert transform as follows

$$(21) \qquad \hat{f}(t) = \cos\alpha f(t) + \sin\alpha H[f(t)]$$

where:

$\hat{f}(t) =$ the phase shifted source wave,

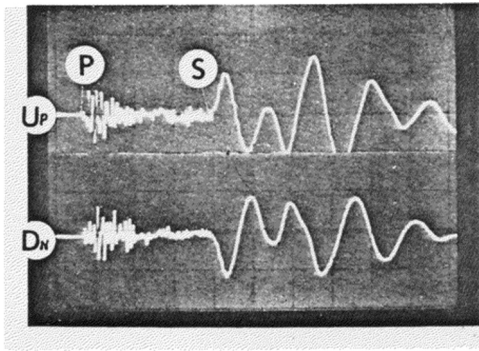$f(t) =$ the original source wave,

$\alpha =$ the phase shift, and

$H[f(t)] =$ the Hilbert transform of the source wave, which introduces a 90° phase shift of a function (i.e., $R = -i$ in Eq 17).

To provide illustrative examples of the phase shifting of seismic source waves due to TIRs, Eq 21 was applied on a 55 Hz Berlage source wave. In **Figs. 13(a)–13(d)**, the solid lines are the Berlage source wave, while the dotted lines the inputted Berlage source wave phase shifted by 60, 90, 120, and 220°, respectively. As is demonstrated in these figures, even though the dominant frequency has been retained, the source waves have been phase shifted within the envelope of the wave packet and the

FIG. 13 (a) Berlage source wave, 60° phase shift. (b) Berlage source wave, 90° phase shift. (c) Berlage source wave, 120° phase shift. (d) Berlage source wave, 220° phase shift.
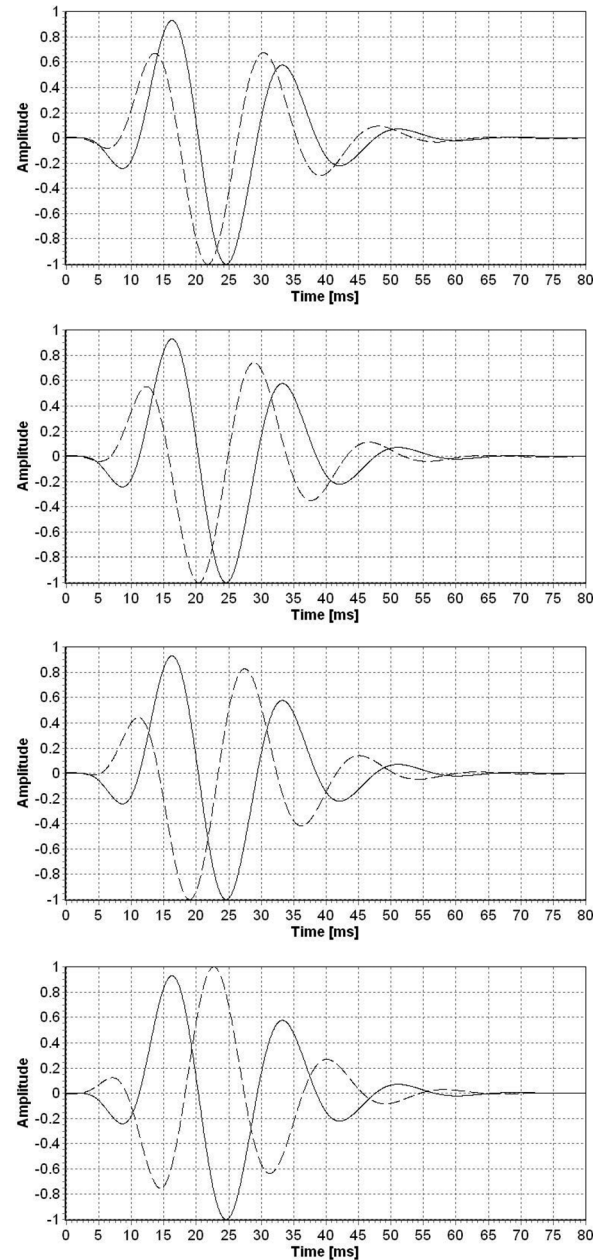
FIG. 14 CST reversible impulse seismic source time plot showing both P and S wave signals and additive noise (ASTM D4428/D4428M-07).

FIG. 15 Reversely polarized DST data showing the time markers for SCPT carried out in stratigraphy containing stone columns (Amini 2006).

minimum and maximum peaks have been modified (i.e., note that the 2 waves have the same arrival time but different phases and minima and maxima) resulting in source wave distortion.

Challenges in Analyzing Seismograms Containing TIRs

### DETERMINATION OF RELATIVE ARRIVAL TIMES

The ability to obtain relative arrival times from seismograms containing TIRs is a very challenging endeavor for both DST and CST. Amini (2005, 2006) carried out extensive work in the analysis of seismic data acquired from SCPT where stone columns were present (and thus TIRs in the seismic data), using the finite difference program FLAC (Fast Lagrangian Analysis of Continua) so that simulated SCPT seismic data could be generated. These simulated data were then compared with field data so that a better understanding of the physical process of ground improvement by vibro-replacement and the corresponding interpretation of SCPT could be obtained.

TIRs are quite common in DST and as a result of that, the first break or arrival is commonly used as a time marker. Unfortunately, estimating arrival times in DST can be quite challenging as the recorded source wave cannot only contain TIRs, but also exhibit P-wave and noise interference. For example, **Fig. 14**, which is taken from ASTM D4428/D4428M-07, illustrates typical seismograms recorded during a DST, clearly showing the presence of TIRs. As is evident from this figure, the P-wave train and measurement noise are superimposed upon the S-wave, making selection of a first arrival a challenging task prone to subjective visualization.

Figure 15 illustrates a vertical seismic profile (VSP) from simulated DST seismograms[6] where stone columns are present (Amini 2006). The identified time markers B–F are not suitable

[6]The simulated seismograms are the responses of imaginary horizontal accelerometers. The simulated trace at each depth is plotted along with its mirror image in order to mimic left and right SH-wave hammer beam impacts.
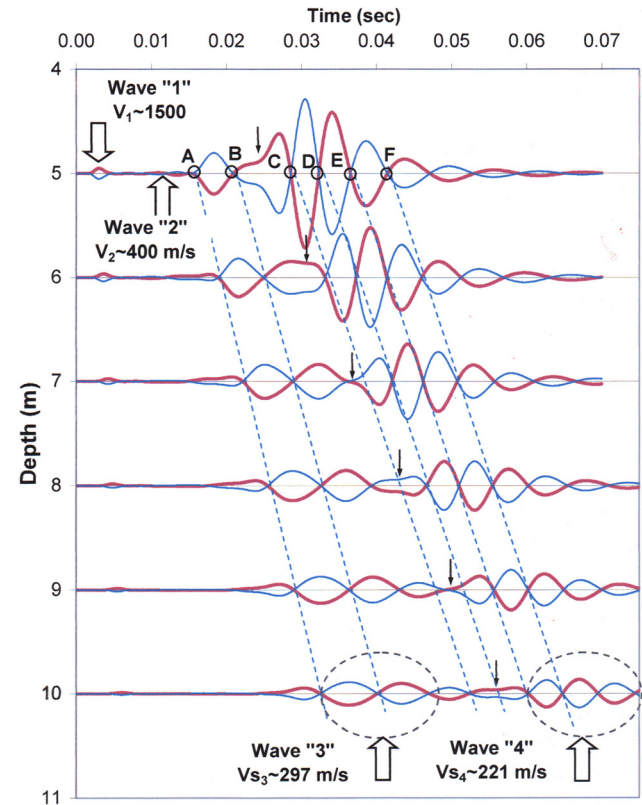
as the basis for analyzing the seismograms due to the fact that their corresponding time location is dependent upon the constructive and destructive interference of the generated source waves, which in turn depend on the geometry of the columns, location of the source, and depth of the seismic adapter. These parameters will be unique for each DST test and therefore a standardized analysis method cannot build on these markers.

It should be noted that the testing configuration implemented to generate **Fig. 15** relied upon exciting both the stone columns and the soil profile under analysis. However, this increases the complexity of the generated source waves considerably, and it is therefore highly recommended that in DST only "point sources" are utilized (with beams of short length in case of SH-wave analysis). In doing so, only the soil under analysis is excited and not the stone columns, and consequently only the direct SH-wave and corresponding reflection will be recorded.

IMPLEMENTATION OF THE CROSS CORRELATION FUNCTION OR CROSS-POWER SPECTRUM

Just as techniques that rely upon identifying reference points or markers cannot be used for seismograms that contain TIRs, techniques that implement the cross correlation function or cross-power spectrum are also problematic for such

FIG. 16

Simulation 1: Berlage source waves with varying phases.
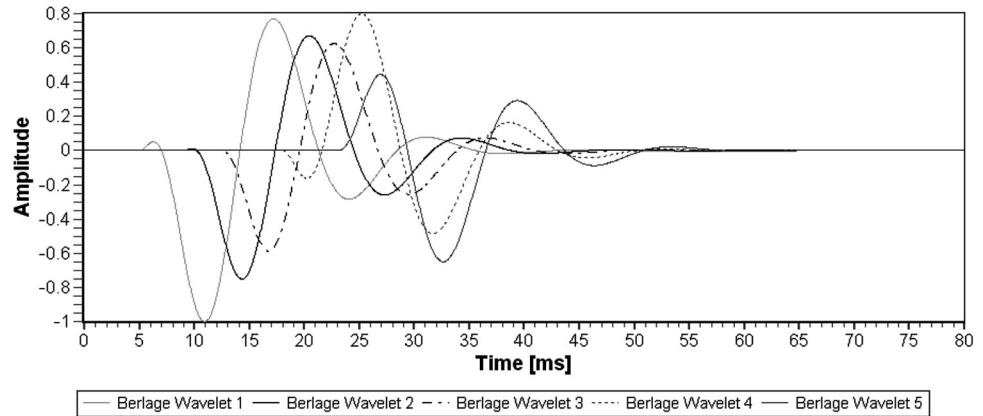
seismograms. Relative arrival time estimates from the cross-spectrum phase estimates cannot be used if any overlapping source wave reflections are present within the recorded seismogram due to the fact that the conflicting phases of the direct wave and overlapping waves will results in an erroneous phase estimate at the dominant source wave frequency. The cross correlation function relies upon dominant amplitude responses; therefore, as long as the first overlapping source waves arrive after the first dominant response of the direct source wave then the cross correlation function can be applied to obtain a relative arrival time. This requires that the seismogram responses after the first arriving dominant response of the direct source are attenuated. However, since this is not necessarily the case for seismograms with TIRs the methodology should be used with the appropriate care.

NUMERICAL EXAMPLE OF SEISMOGRAMS WITH TIRS

Simulated seismograms containing TIRs can also be used to demonstrate the effect and corresponding challenges of these TIRs when carrying out DST and CST. In seismology, the recorded time series, $z(t)$, is defined to be the linear convolution of the source wavelet, $S(t)$, with the earth's reflection coefficients, $\mu(t)$, with additive measurement noise, $v(t)$. The mathematical representation of this relationship is given as (Ulrych and Sacchi 2005; Baziw 2006, 2007, 2011)

$$(22) \qquad z(t) = \int_0^t \mu(t)S(t - \tau)d\tau + v(t)$$

The discrete representation of Eq 22 is given as

$$(23) \qquad z(k) = \sum_{i=1}^{k} \mu(i)S(k - i) + v(k), \quad k = 1, 2 \ldots N$$

Equations 22 and 23 are applicable if the source wave is stationary. However, in case of TIRs, the direct and reflected source waves are time variant (phase distortion) and therefore it is not

possible to implement Eq 23 to generate synthetic seismograms. Instead, these synthetic seismograms have to be based on the fact that in reflection seismology, the discrete convolution operation can be represented as the summation of several source waves of differing arrival times.

To generate synthetic seismograms for a DST VSP, five Berlage source waves were generated and superimposed at depths of 5, 6, and 7 m. These waves are defined as (Baziw 2006, 2007, 2011)

$$(24) \qquad w(t) = AH(t)t^n e^{-\alpha t} \cos(2\pi ft + \emptyset)$$

where $H(t)$ is the Heaviside unit step function [$H(t) = 0$ for $t \leq 0$ and $H(t) = 1$ for $t > 0$]. The amplitude modulation component is controlled by two factors: the exponential decay term α and the time exponent n. These parameters are considered to be nonnegative real constants. All simulated waves had the common values of $f = 70$ Hz, $n = 2$, and $\alpha = 270$ specified. The phase values are set at $\emptyset = 20, 40, 140,$ and $250°$, respectively. The arrival times[7] and maximum amplitudes were set as follows for the five Berlage source waves:

- at a depth of 5 m: (5 ms, 1), (8 ms, 0.75), (11 ms, 0.625), (17 ms, 0.8), and (22 ms, 0.65), respectively (see **Fig. 16**).
- at a depth of 6 m: (9 ms, 1), (14 ms, 0.75), (17 ms, 0.625), (21 ms, 0.8), and (24 ms, 0.65), respectively (see **Fig. 17**).
- at a depth of 7 m: (14 ms, 1), (17 ms, 0.75), (21 ms, 0.625), (24 ms, 0.8), and (29 ms, 0.65) respectively (see **Fig. 18**).

For each depth superposition of the source waves is shown with the reflection coefficients to allow for the visualization of the arrival time and maximum amplitude values (**Figs. 19**, **20**, and **21** for the depth of 5, 6, and 7 m, respectively).

It is clear from these figures that there is significant distortion of the direct source wave due to the superposition of the

---

[7]The first 24 ms of data of seismograms 1, 2, and 3 have been removed due to the fact that no seismic data is contained within the first 24 ms and we are only interested in relative arrival times between depths 5 to 6 m and 6 to 7 m.
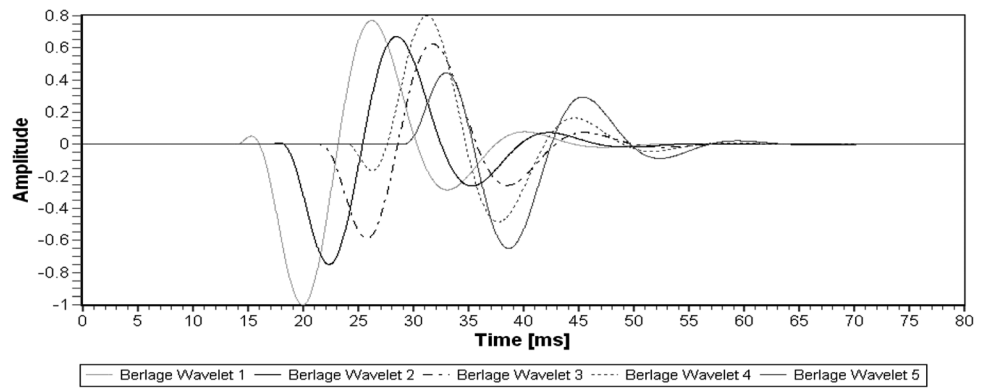
FIG. 17

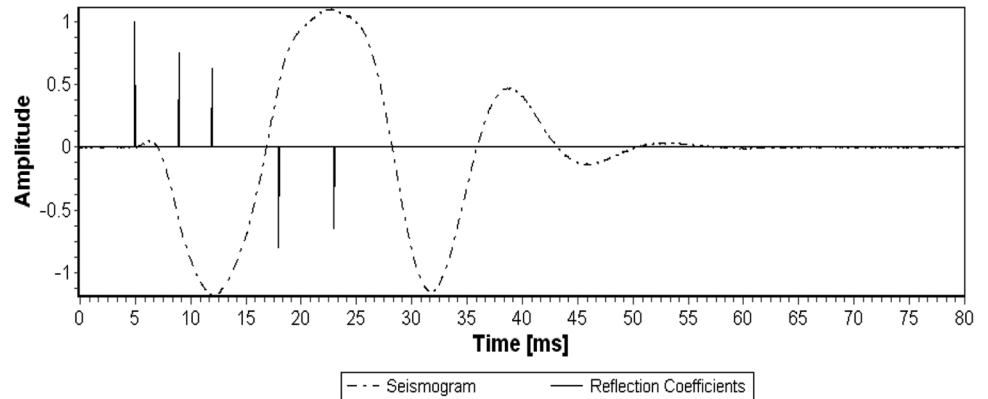Simulation 2: Berlage source waves with varying phases.
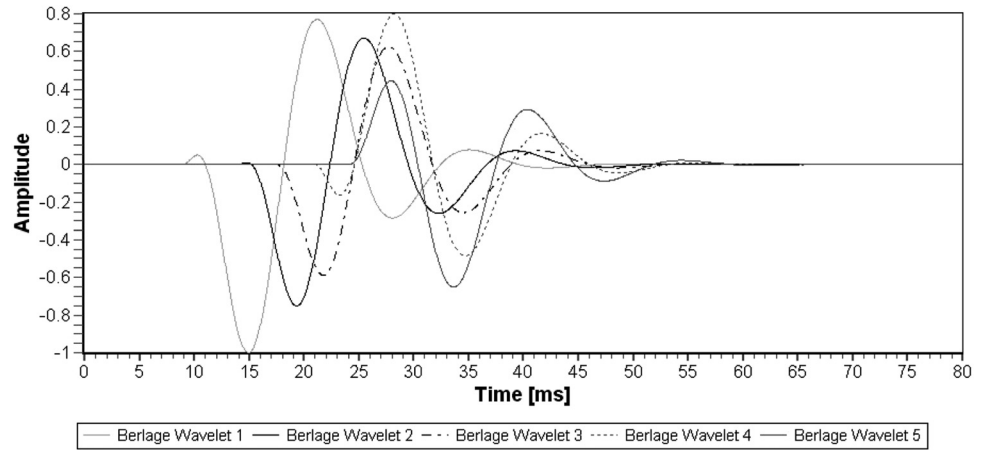
FIG. 18

Simulation 3: Berlage source waves with varying phases.

FIG. 19

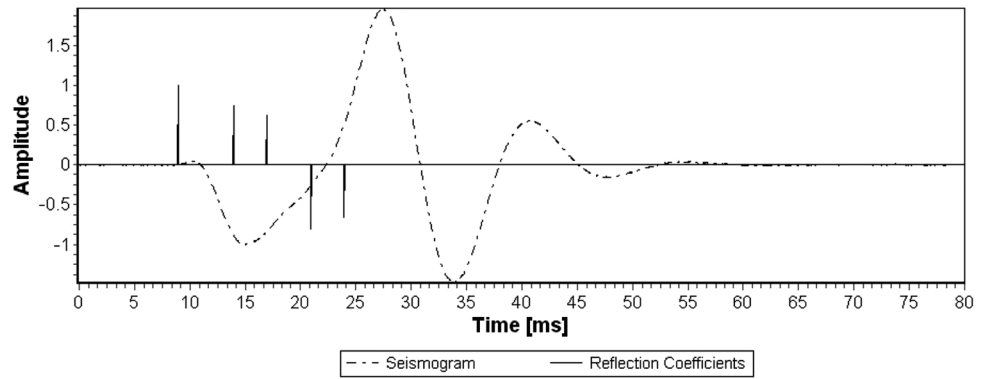Superposition of Berlage source waves illustrated in **Fig. 16**.
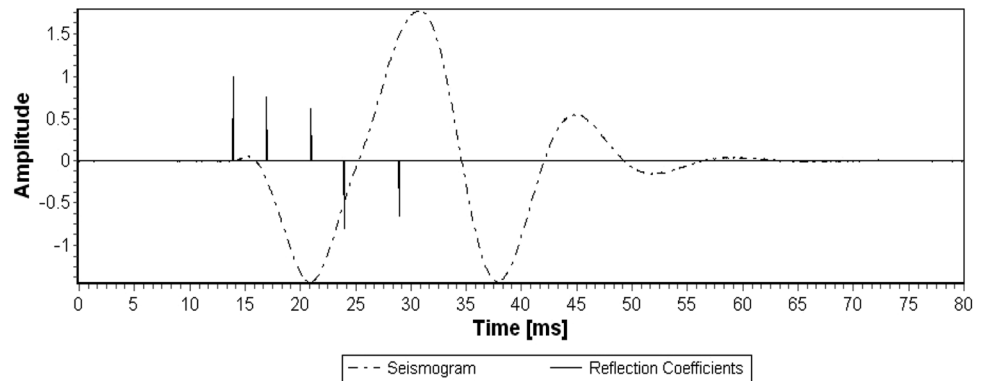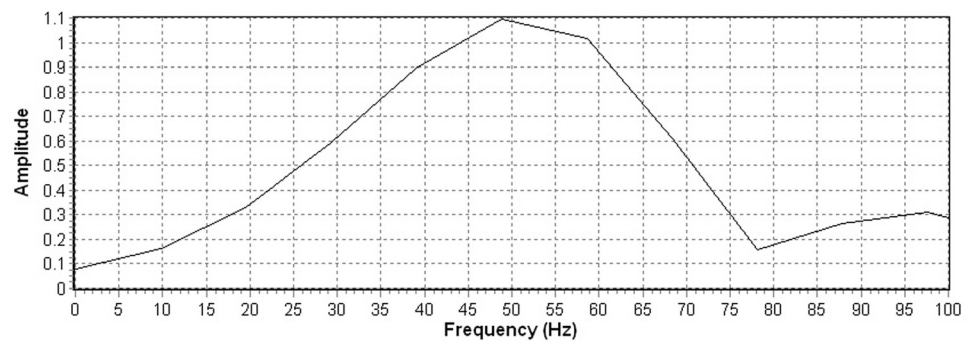
FIG. 20

Superposition of Berlage source waves illustrated in **Fig. 17**.

FIG. 21

Superposition of Berlage source waves illustrated in **Fig. 18**.
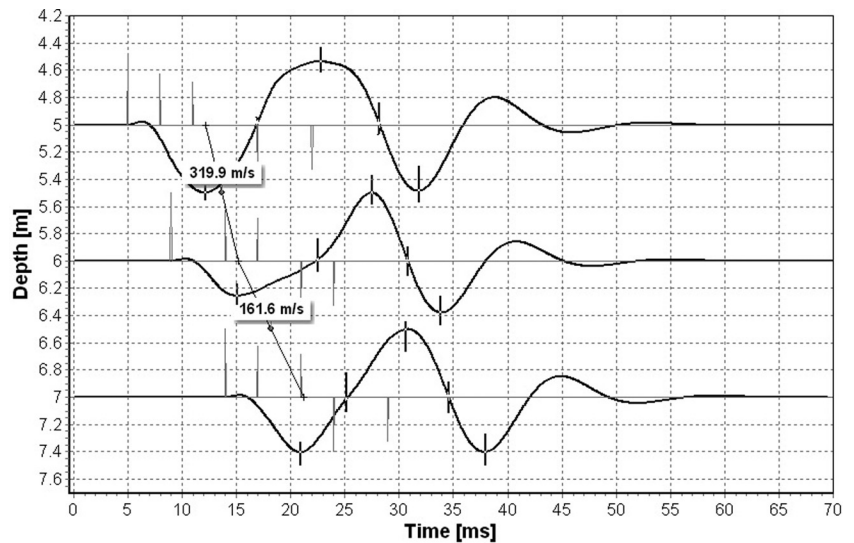

FIG. 22

Fourier transform for seismogram illustrated in **Fig. 17**. The dominant frequency has been lowered to 49 Hz from the original Berlage source wave peak frequency of 70 Hz.

FIG. 23

VSP of simulated seismograms with corresponding reflection coefficients (grey time series) and time markers (denoted as short bold lines). The time markers are shown along with the first peak estimated interval velocities.

TIRs. This becomes even more evident when comparing the FFT with the original source wave. For example, **Fig. 22** illustrates the FFT for the seismogram illustrated in **Fig. 19**, and it is obvious that the 70 Hz dominant frequency of the Berlage source wave has been lowered to 49 Hz due to the overlapping TIRs.

Figure 23 illustrates the VSP of the simulated seismograms of **Figs. 19**, **20**, and **21** with the corresponding reflection coefficients and time markers (denoted as short bold lines) of First Peak (FP), First Crossover (FC), Second Peak (SP), Second Crossover (SC). For this test simulation, a source-sensor radial offset of 1.5 m was assumed; therefore, referring to **Fig. 1** and Eq 1, the slant distances, d_i, for the simulation depth of 5, 6, and 7 m are 5.22, 6.18, and 7.16 m, respectively. Using Eq 1 and assuming a straight ray travel path (i.e., no refraction) the first arriving direct source wave interval velocities can be calculated as $V_{5-6} = (6.18 - 5.22)/(9 - 5) = 241 m/s$ for depth interval 5 to 6 m and $V_{6-7} = (7.16 - 6.18)/(14 - 9) = 196 m/s$ for depth interval 6 to 7 m.

Figure 23 also shows the trend lines based upon the FP time markers, which translate to estimated interval velocities of $V_{5-6} = 320$ and $V_{6-7} = 162 m/s$. **Table 2** summarizes the estimated interval velocities and associated % error for time makers FP, FC, SP, and SC, and shows that these estimated interval velocities are clearly unreliable. These and similar test bed simulations make it clear that time markers FP, FC, SP, and SC cannot be used when deriving interval velocities when TIRs are present within the recorded seismograms.

However, while it is clear that the interval velocities should be calculated based on the First Arrival (FA) time marker, **Figs. 24** and **25** demonstrate the difficulties in obtaining these FA time markers. **Figure 24** shows the seismogram shown in **Fig. 23** with superimposed Gauss–Markov measurement noise (Baziw 2006, 2007) with a time constant of 1 ms and variance of 0.02 (to simulate the effects of the first arriving source waves (e.g., P-wave), near field effects, and ambient noise) and overall white noise with variance 0.001 (to account for possible electrical noise). **Figure 25** illustrates the seismograms shown in **Fig. 24** with a 150 Hz low pass filter applied to noisy traces. **Figure 25** also shows the trend lines based upon the FA time marker, which translate in estimated interval velocities of $V_{5-6} = 140$ and $V_{6-7} = 257 m/s$. These interval velocities have an error of 42 and 31%, respectively, and are therefore again unacceptable.

REAL EXAMPLE OF SEISMOGRAMS WITH TIRS

The real DST data outlined in this section (the so-called SC 64) was acquired during a SCPT in New Zealand near the Tauranga

TABLE 2   Time markers estimated interval velocities and associated percent errors.

Depth Interval (m)	FP Interval Velocity Estimate (FPIVE) (m/s)	FPIVE Percent Error[a] (%)	FC Interval Velocity Estimate (FCIVE) (m/s)	FCIVE Percent Error* (%)	SP Interval Velocity Estimate (SPIVE) (m/s)	SPIVE Percent Error[a] (%)	SC Interval Velocity Estimate (SCIVE) (m/s)	FCIVE Percent Error[a] (%)
5–6	320	32.3	176	27	213	12	454	88
6–7	162	16.8	333	70	268	37	224	14

[a]Percent error = (Estimate—true) × 100/true.

FIG. 24

Simulated seismograms shown in **Fig. 23** (black traces) superimposed upon the same seismograms which have additive measurement noise (grey traces).
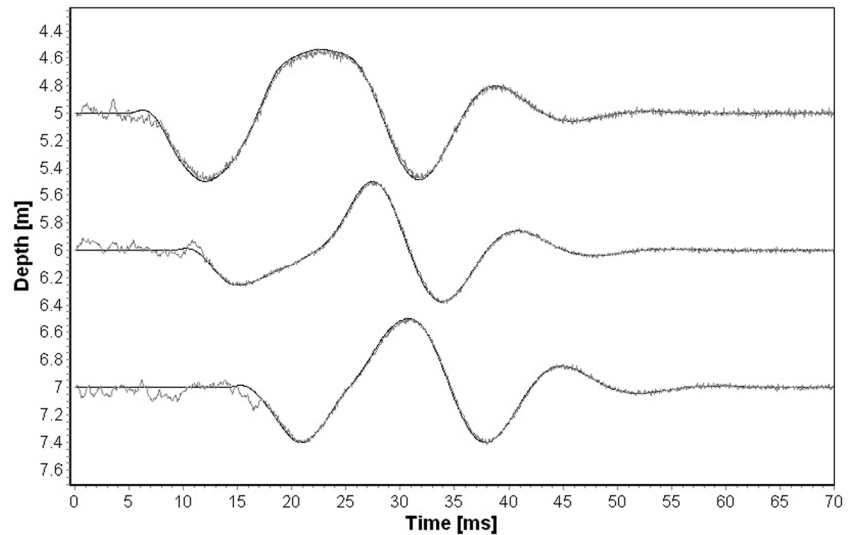
Eastern Motorway by Perry Drilling Ltd. of Tauranga New Zealand. The (SH) source waves were generated with a sledge hammer horizontally impacting point source steel beams located underneath the outriggers (2.3 ms from the center of the rod string) and an electrical contact trigger. Two stacked SH source waves were generated for each depth increment.

The SCPT was performed approximately 4 to 5 m to the east of a pond that is 1 to 2 m deep. The test was conducted 1 m below the bund surrounding the pond, which is used as an access road. This bund is constructed of dense material, and thus acted as a strong reflector of the SH source waves.

Figure 26 shows the raw time series data captured with the SH source located on the right side of the SC. **Figure 27** shows the same seismic data, but with a low pass 140 Hz zero phase shift frequency filter applied. As is evident from **Figs. 26** and **27**, there are source reflections multiples present within the captured time series data, and the short vertical lines in **Fig. 27** denote locations of possible deconstructive interference between the direct source wave and overlapping source wave reflections.

For the depths between 2 and 4 ms, **Fig. 28** illustrates the first trough and first peak time markers (denoted by short vertical solid black lines). Due to the relatively low bandwidth of the source wave and constructive/destructive interference of the reflections the peak value time marker determination is prone to human bias, which is illustrated with a so-called time marker window of ambiguity (denoted by the dashed lines). However, apart from this window of ambiguity, the use of time markers is problematic: **Table 3** outlines the estimated interval velocities
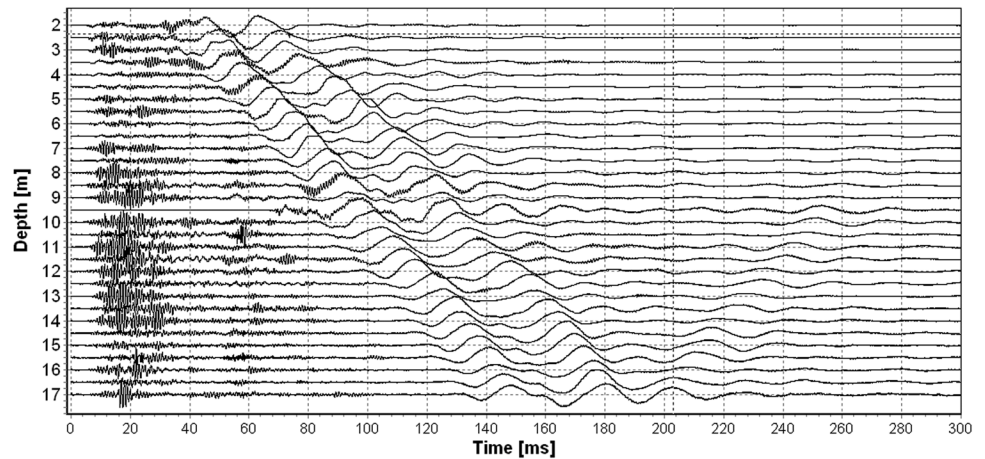
FIG. 25

Seismograms shown in **Fig. 24** with a 150 Hz low pass filter applied to noisy traces. The illustrated trend lines provide for interval velocities of 140 m/s and 257 m/s for depth interval 5 to 6 m and 6 to 7 m.
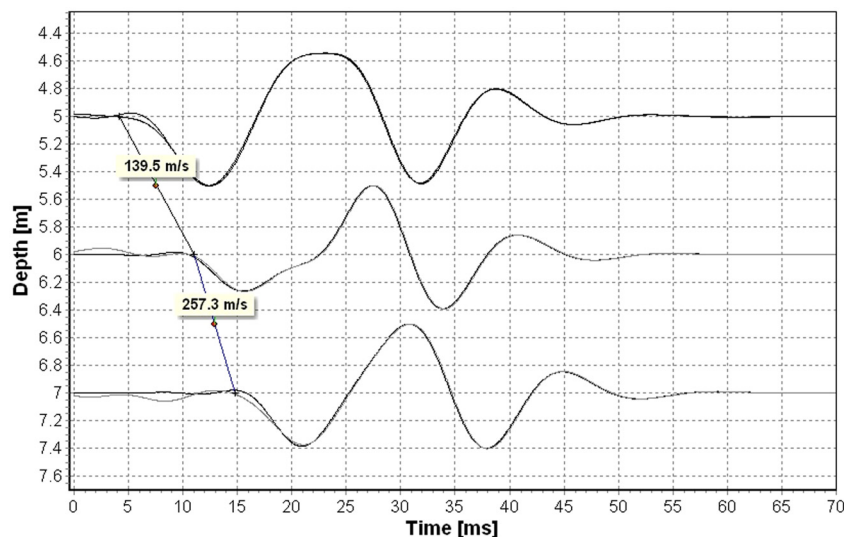
FIG. 26

Raw VSP from SCPT hole SC 64.

from the VSP illustrated in **Fig. 27** based on either the first trough or the first peak time makers. As is shown in this table, the difference in outcome can be substantial (in this case up to nearly 80 %) due to the constructive/destructive of the source wave reflections.

RECOMMENDED ANALYSIS METHOD FOR SEISMOGRAMS WITH TIRS

The authors believe that seismic signal processing techniques which attempt to isolate the direct source wave from the reflected source waves should be investigated and developed for the case of DST and CST seismograms containing TIRs. These techniques would require time variant BSD (BSDtv) analysis methodologies (Baziw 2006, 2007, 2011; Gholami and Sacchi 2012; Ulrych and Sacchi 2005). The BSDtv methodology not only addresses the case where both $S(t)$, and $\mu(t)$ are unknown

in Eqs 22 and 23, but also cover the non-stationary aspect of TIRs.

It goes beyond the scope of this paper to discuss the BSDtv methodology in detail, but the authors have been working on an algorithm for processing seismograms containing TIRs that would extract the direct source waves. Direct and relative arrival times and corresponding interval velocities are then readily obtained from these extracted source waves. Details of this algorithm will be published in a separate paper later this year, but the algorithm builds on the powerful BSD algorithm referred to as Principle Phase Decomposition (PPD) (Baziw 2006, 2007, 2011).

Just as in the BSD algorithm, in the BSDtv algorithm, the source wave is uniquely modeled as an Amplitude Modulated Sinusoid (AMS), which has been demonstrated to be a highly robust and accurate approximation for many analytical representations of seismic source waves. In addition, the AMS wave
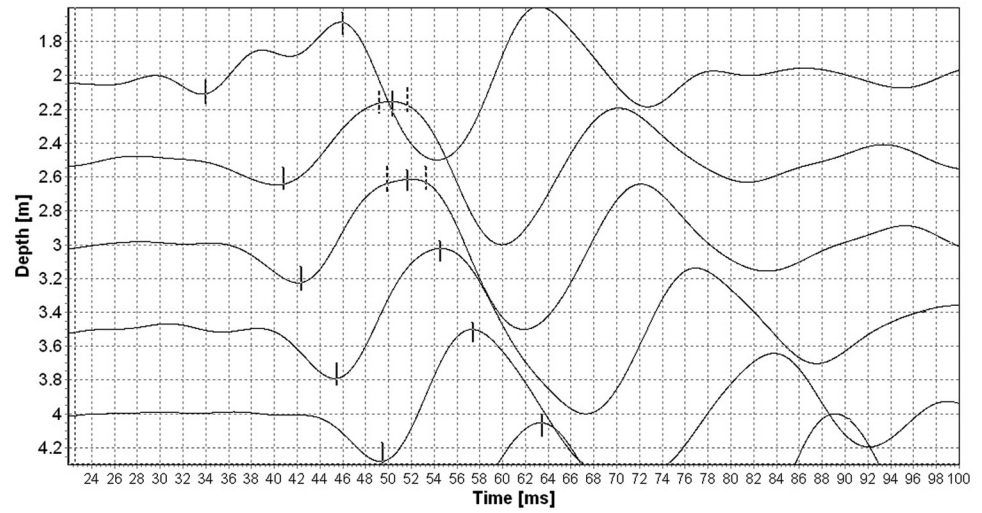
FIG. 27

VSP illustrated in **Fig. 26** with a 140 Hz low pass filter applied. There is clear evidence of overlapping source waves denoted by short vertical lines.
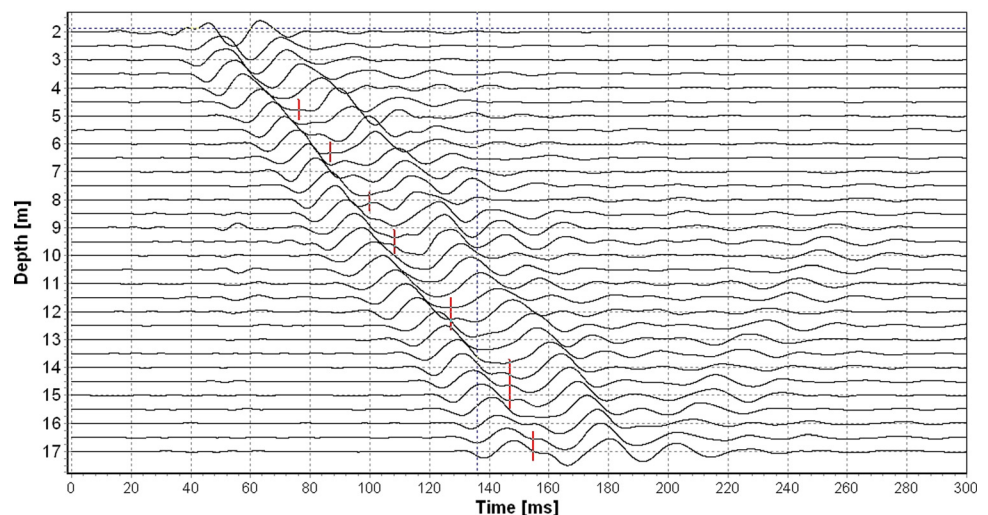
FIG. 28

Illustration of time markers first trough and first peak (denoted by short vertical solid black lines). The dashed short vertical lines identify time marker windows of ambiguity.


TABLE 3   Estimated interval velocity estimates for SCPT site SC 64.

Interval Depth (m)	First Trough Trend Line Velocity Estimate (m/s)	First Peak Trend Line Velocity Estimate (m/s)	Difference in Velocity Estimate (m/s)	Average Velocity Estimate (m/s)	Percent[a] Difference Estimate (%)
2.0–2.5	50	74	24	62	38.7
2.5–3.0	277	292	15	284.5	5.3
3.0–3.5	130	157	27	143.5	18.8
3.5–4.0	101	146	45	123.5	36.4
4.0–4.5	90	75	15	82.5	18.2
4.5–5.0	98	110	12	104	11.5
5.0–5.5	112	116	4	114	3.5
5.5–6.0	174	106	68	140	48.6
6.0–6.5	106	124	18	115	15.7
6.5–7.0	133	203	70	168	41.7
7.0–7.5	185	100	85	142.5	59.6
7.5–8.0	171	254	83	212.5	39.1
8.0–8.5	187	133	54	160	33.8
8.5–9.0	169	178	9	173.5	5.2
9.0–9.5	293	189	104	241	43.2
9.5–10.0	123	116	7	119.5	5.9
10.0–10.5	158	163	5	160.5	3.1
10.5–11.0	113	122	9	117.5	7.7
11.0–11.5	107	141	34	124	27.4
11.5–12.0	122	123	1	122.5	0.8
12.0–12.5	82	74	8	78	10.3
12.5–13.0	187	180	7	183.5	3.8
13.0–13.5	139	120	19	129.5	14.7
13.5–14.0	141	324	183	232.5	78.7
14.0–14.5	206	129	77	167.5	46
14.5–15.0	123	185	62	154	40.3
15.0–15.5	179	138	41	158.5	25.9
15.5–16.0	156	294	138	225	61.3
16.0–16.5	239	150	89	194.5	45.8
16.5–17.0	203	207	4	205	2

[a]Percent Difference: the difference between two values divided by the average of the two values.

FIG. 29

Illustrating the constant AMT for the Berlage source waves shown in **Fig. 16**. Berlage Wavelets 1 to 5 have the same 5 ms arrival time specified so that the constant AMT can be demonstrated.
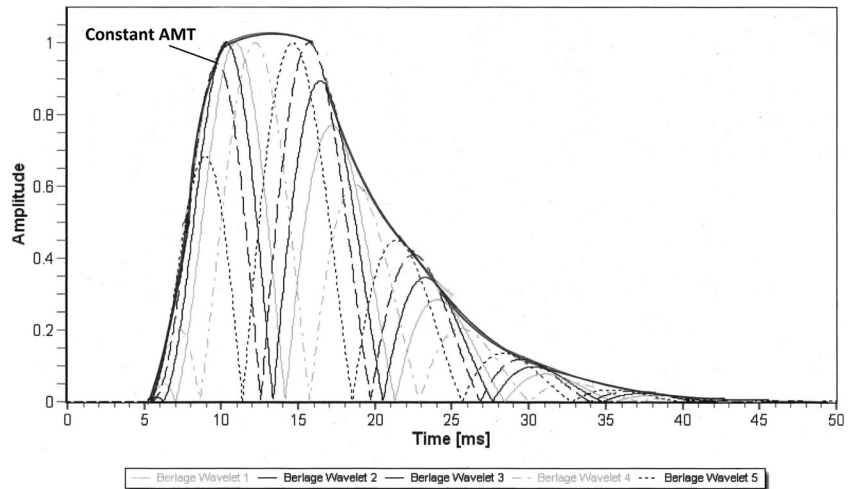
has proven very accurate in modeling seismic data acquired during passive seismic monitoring (Baziw et al. 2002b, 2004 b; Baziw and Verbeek 2012b) and vertical seismic profiling (Baziw 2011). In general terms, the AMS source wave is defined to be a sinusoid with a dominant frequency and phase modulated by an Amplitude Modulating Term (AMT).

The BSDtv algorithm uses the same a priori information as the BSD algorithm, but in addition the following a priori information for TIRs is incorporated:

- although the phase of the source wave changes for each reflection, the dominant frequency remains the same;
- the time width of the source wave remains constant;
- the reflected source waves are modeled as AMSs;

- the AMTs of the direct and reflected source waves remain constant.

Figure 29 illustrates the concept of a constant AMT for TIRs. In this figure, the absolute amplitudes of the source waves outlined in **Fig. 16** are superimposed with an identical arrival time of 5 ms specified for each wave. The dark AMT outline shown in **Fig. 29** illustrates that all of the TIRs can be modeled as AMSs where there is a constant AMT envelop. This is why the AMT component of the direct and reflected source waves are assumed constant in the BSDtv algorithm. In general terms, the proposed BSDtv algorithm for processing seismograms containing TIRs would extract the direct source waves. Direct and relative arrival times and corresponding interval velocities are

FIG. 30

VSP (with associated trend lines) of estimated Berlage Waves utilizing a BSDtv algorithm.
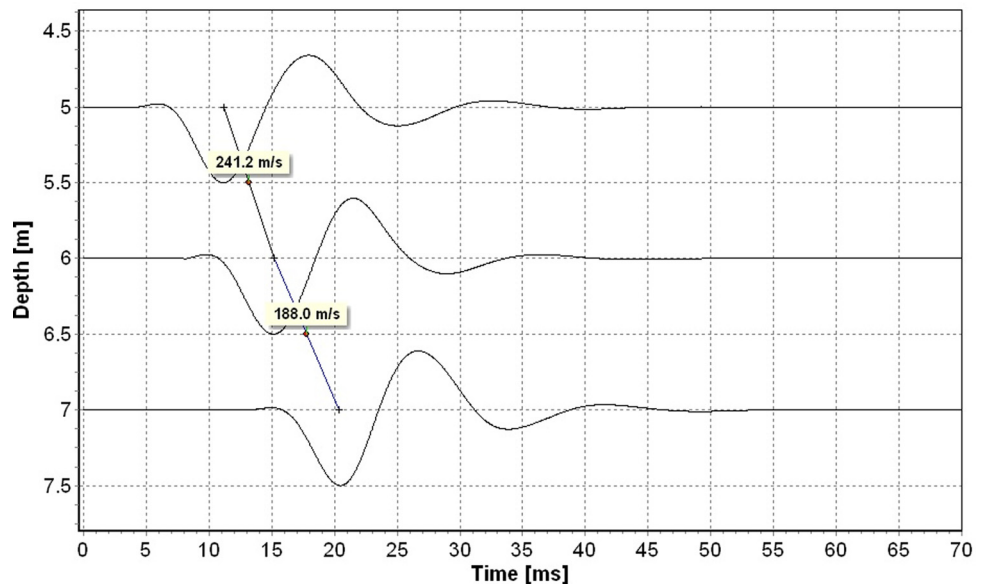
then readily obtained from these extracted source waves. In addition, the estimated reflection coefficients identify and quantify the vertical inclusions and bounding geological layers.

A preliminary example of the BSDtv algorithm is shown in **Fig. 30**, which shows the source wave extracted by the algorithm from the data shown in **Fig. 23**. Once the source wave is available, the common data analysis methods can be applied to determine the direct and relative arrival times as well as the corresponding interval velocities.

Conclusions

As outlined in this paper, a very common and important problem encountered in DST and CST is the recording of seismograms which contain Total Internal Reflections (TIRs). TIRs arise when the incident angle exceeds the critical angle, and they are associated with reflected source wave distortions due to the fact that the reflection coefficients become complex. TIRs are typical in CST investigations (since horizontally travelling source waves have high angles of incidence on bounding stratigraphic layers), while in DST investigations, TIRs are encountered whenever there are significant man-made structures (piles, stone columns, and deep underground structures such as deep basements, parking garages, and dam structures).

Typical DST and CST interval velocity estimation techniques which rely upon the implementation of the cross correlation function, cross-power spectrum and/or time markers are unlikely to provide acceptable estimates when TIRs are present within the seismograms.

More advance data processing techniques which attempt to isolate the direct source wave from the reflected source waves (such as the time variant BSD (BSDtv) analysis methodology) should be investigated and developed for the case of DST and CST seismograms containing TIRs.

References

Aki, K. and Richards, P.G., 2002, *Quantitative Seismology*, 2nd ed., University Science Books, Sausalito, CA.

Amini, A., 2006, "Application of Seismic Cone for Characterization for Ground Improved by Vibro-Replacements" Ph.D. thesis, University of British Columbia, Vancouver, BC.

Amini, A. and Howie, J. A., 2005, "Numerical Simulation of Downhole Seismic Cone Signals," *Can. Geotech. J.*, Vol. 42, No. 2, pp. 574–586.

Andrus, R. D. and Stokoe, K. H., II, 2000, "Liquefaction Resistance of Soils From Shear-Wave Velocity," *ASCE J. Geotech. Geoenviron. Eng.*, Vol. 126, No. 11, pp. 1015–1025.

Andrus, R. D., Stokoe, K. H. and Chung, R. M., 1999, "Draft Guidelines for Evaluating Liquefaction Resistance Using Shear Wave Velocity Measurements and Simplified Procedures," *NISTIR 6277*, National Institute of Standards and Technology, Gaithersburg, MD.

ASTM D4428/D4428M, 2013: Standard Test Methods for Crosshole Seismic Testing, *Annual Book of ASTM Standards*, ASTM International, West Conshohocken, PA.

ASTM D7400, 2013: Standard Test Methods for Downhole Seismic Testing, *Annual Book of ASTM Standards*, ASTM International, West Conshohocken, PA.

Baziw, E., 1993, "Digital Filtering Techniques for Interpreting Seismic Cone Data," *ASCE J. Geotech. Eng.*, Vol. 119, No. 6, pp. 998–1018.

Baziw, E., 2002, "Derivation of Seismic Cone Interval Velocities Utilizing Forward Modeling and the Downhill Simplex Method," *Can. Geotech. J.*, Vol. 39, pp. 1–12.

Baziw, E. and Ulrych, T. J., 2006, "Principle Phase Decomposition—A New Concept in Blind Seismic Deconvolution," *IEEE Trans. Geosci. Remote Sens.*, Vol. 44, No. 8, pp. 2271–2281.

Baziw, E., 2007, "Implementation of the Principle Phase Decomposition Algorithm," *IEEE Trans. Geosci. Remote Sens.*, Vol. 45, No. 6, pp. 1775–1785.

Baziw, E., 2011, "Incorporation of Iterative Forward Modeling Into the Principle Phase Decomposition Algorithm for Accurate Source Wave and Reflection Series Estimation," *IEEE Trans. Geosci. Remote Sens.*, Vol. 49, No. 2, pp. 650–660.

Baziw, E. and Verbeek, G., 2012, "Deriving Interval Velocities from Downhole Seismic Data," *Geotechnical and Geophysical Site Characterization 4*, P. W. Mayne, Ed., CRC Press, Boca Raton, FL, pp. 1019–1024.

Ballard, R. F., Jr., 1976, "Method for Crosshole Seismic Testing," *ASCE Geotech. Eng. Div.*, Vol 102, No. GT12, pp. 1261–1273.

Campanella, R. G., Robertson, F. T. C., and Gillespie, D., 1986, "Seismic Cone Penetration Test," *Proceedings of the INSITU86, American Society of Civil Engineers (ASCE) Geotechnical Special Publication. No. 6*, ASCE, Reston, VA, pp. 116–130.

Finn, W. D. L., 1984, "Dynamic Response Analysis of Soils in Engineering Practice," *Mechanics of Engineering Materials*, Wiley, New York, Chap. 13.

Fokkema, J. T. and Ziolkowski, A., 1987, "The Critical Reflection Theorem," *Geophysics*, Vol. 52, No. 7, pp. 965–972.

Gholami, A. and Sacchi, M. D., 2012, "A Fast and Automatic Sparse Deconvolution in the Presence of Outliers," *IEEE Trans. Geosci. Remote Sens.*, Vol. 50, No. 10, pp. 4105–4116.

Ishihara, K., 1982, "Evaluation of Soil Properties for Use in Earthquake Response Analysis," *Proceedings of the International Symposium on Numerical Models in Geomechanics*, Zurich, Switzerland, September 13–17, pp. 237–259.

Kanasewich, E. R., 1981, *Time Sequence Analysis in Geophysics*, 3rd ed., The University of Alberta Press, Edmonton, AB.

Robinson, E. A., and Treitel, S., 1980, *Geophysical Signal Analysis*, Prentice Hall, Inc., Englewood Cliffs, NJ, pp. 219–224.

Sheriff, R. E. and Geldart, L. P., 1982, *Exploration Seismology*, Vol. 1, 1st ed., Cambridge University Press, Cambridge, UK.

Shearer, P. M., 1999, *Introduction to Seismology*, Cambridge University Press, Cambridge, UK.

Ulrych, T. J. and Sacchi, M. D., 2005, *Information-Based Inversion and Processing With Applications*, 1st ed., Elsevier, Amsterdam, The Netherlands.

William, H. P., Teukolsky, S. A., Vetterling, W. T. and Flannery, B. P., 2007, *Numerical Recipes, The Art of Scientific Computing*, 3rd ed., Cambridge Univesity Press, New York.